THE ASTROPHYSICAL JOURNAL, 465:216–230, 1996 July 1

A TWO-WIND INTERACTION MODEL FOR PROPLYDS

W. J. HENNEY, A. C. RAGA, S. LIZANO, AND S. CURIEL
Instituto de Astronomía, Universidad Nacional Autonoma de Mexico, Apdo. Postal 70-264, 04510 Mexico D. F., Mexico
Received 1995 November 22; accepted 1996 January 10

ABSTRACT

Recent *HST* observations of the Orion Nebula show the presence of compact ($\sim 2''$) emission-line objects ("proplyds") with bowlike morphologies and tails pointing away from the θ^1C Ori star. We model these objects as the result of the interaction between the fast wind from θ^1C Ori and slow dense winds from accretion disks around young, low-mass stars, which are photoevaporated by the ionizing radiation coming from this massive star.

We develop a fully analytic model for this two-wind interaction, which shows that depending on the value of the dimensionless parameter $\lambda = F_0 c_0/n_w v_w^2$, where c_0 is the sound speed of the ionized gas, F_0 is the ionizing photon flux impinging on the surface of the accretion disks, and $n_w v_w^2$ is the specific momentum flux of the wind from θ^1C Ori, both "choked" subsonic (low λ) solutions and "free" supersonic (high λ) solutions can be found. We argue that for the case of θ^1C Ori, this second supersonic regime is relevant.

For the supersonic regime, we find that both the properties of the exciting star (θ^1C Ori) and the size of the accretion disk that ejects the photoevaporated wind enter the solution only as a direct scaling of the size of the proplyd. The only physical parameter with a more complex effect on the problem is the orientation between the axis of the accretion disk and the direction to θ^1C Ori.

We finally use this analytic model to produce predicted emission measure maps (which are directly compared to the *HST* images of O'Dell & Wen 1994). A good qualitative agreement is found at least for some of the proplyds observed in the Orion Nebula.

Subject headings: H II regions — hydrodynamics — ISM: individual (Orion Nebula) — ISM: jets and outflows — stars: individual (θ^1 Orionis C) — stars: mass loss

1. INTRODUCTION

Recent observations obtained with the *Hubble Space Telescope* (O'Dell & Wen 1994; O'Dell, Wen, & Hu 1993) show the presence of a number of elongated emission-line knots in the region surrounding θ^1C Ori. Some of these clumps have positions that coincide with the previously detected "LV knots" (Lacques & Vidal 1979) or with "PIGs" (partially ionized globules) detected at radio wavelengths (Churchwell et al. 1987).

A possible interpretation of these objects (McCullough et al. 1995) is that they correspond to the wind from a compact, molecular core, which is being photoevaporated by the ionizing radiative field from θ^1C Ori. Even though this interpretation is promising, it appears to have two drawbacks. First, some of the proplyds (e.g., the LV knots) surround clearly visible stars, while McCaughrean & Stauffer (1994) find that in virtually all proplyds a central young star is visible in the near-infrared. From this one would conclude that a high extinction core is not present in these objects.

Second, the interaction of an initially spherical cloud core with an incident radiative field (and possibly also with a wind from the same source) will lead to structures that are symmetrical with respect to the axis joining the center of the core and the massive star. However, many of the observed proplyds have a highly asymmetric shape, and some objects have partially symmetric structures with axes that deviate considerably from the direction to the ionizing photons/wind source.

A natural way to explain such asymmetries is to assume that the cloud core is aspherical, with a symmetry axis that is not necessarily parallel to the direction toward the source. In this scenario, the photoevaporated wind comes from an accretion disk surrounding a low-mass star (O'Dell et al. 1993; McCullough et al. 1995; Lizano et al. 1996). This scenario has the advantage of producing a proplyd with a possibly visible central star (as the flattened nature of the envelope allows direct lines of sight to the star).

Following this idea, in this paper we develop an analytic model of the interaction of a photoevaporated wind from an accretion disk, powered by the ionizing radiative field from an external source, with a powerful stellar wind from this source (§ 2). The resulting two-wind interaction can have very different characteristics depending on the relative values of the photon and mass fluxes from the external source. The two resulting regimes are described in §§ 3 and 4. The values of the model parameters that are deduced from the observations of the Orion proplyds are discussed in § 5. Finally, a comparison between observed and predicted Hα intensity maps is presented in § 6.

2. GENERAL CONSIDERATIONS

Proplyds are small emitting knots with characteristic radii $\sim$20–100 a.u. and very large Hα luminosities $\sim$0.01–0.1 $L_\odot$ (McCullough et al. 1995). These general characteristics can be straightforwardly reproduced with models of photoevaporated compact clumps or disks.

To a certain extent, the observations of proplyds appear to favor a "photoevaporated disk" over a "clump" model for two reasons. First, several proplyds show a morphology that is not symmetrical with respect to the direction to θ^1C Ori, considered to be the main exciting source. These asymmetries cannot be reproduced with a model of the photoevaporation of an initially spherical clump, and are a clear feature of what is to be expected for the photoevaporation of a flattened, disklike structure of arbitrary orientation.

Second, the fact that the embedded stars are optically visible in some of the proplyds (e.g., in the LV knots) can also be interpreted as a possible indication of the presence of a flattened circumstellar structure.

The most striking morphological properties of these objects are their "tails," which extend radially outward from the direction to θ^1C Ori for up to ~ 500 a.u. from the "heads" of the proplyds. In order to understand this phenomenon, it is necessary to find a mechanism that can redirect the photoevaporated wind, which will initially be streaming toward the source of ionizing radiation, away from this source.

The two obvious candidates for solving this "confinement problem" are the radiation pressure of the photoionizing field and the ram pressure of the wind from θ^1C Ori. In order to choose between these two possible confinement processes, let us present some general considerations, which are independent of the precise geometry of the photoevaporated structure (applying to both disks and clumps).

Every ionizing photon that arrives to the surface of the neutral disk (or clump) liberates an ion. If one assumes that the photoevaporated material is ejected at the isothermal sound speed of the ionized gas c_0 (~ 10 km s^{-1}), then, in a steady state,

$$F_0 \approx \frac{\rho_0 c_0}{m}, \tag{1}$$

where F_0 is the ionizing photon flux arriving to the ionization front (which, for simplicity, we assume to be perpendicular to the direction toward the photon source), ρ_0 is the density of the photoevaporated wind at this surface, and $m \approx 1.3 m_{\rm H}$ is the average mass per atom or ion. Therefore, the gas pressure at the base of the photoevaporated wind is given by

$$P_{\rm gas} = \rho_0 c_0^2 \approx m c_0 F_0 . \tag{2}$$

The pressure of the ionizing radiation acts on the region close to the base of the photoevaporated wind (i.e., in the region close to the ionization front), where the radiation is absorbed. The radiation pressure has a value

$$P_{\rm rad} = \frac{F_0 \langle h\nu \rangle}{c} \approx \frac{F_0 h\nu_0}{c}, \tag{3}$$

where c is the speed of light, and the average energy of the ionizing photons $\langle h\nu \rangle \approx h\nu_0$, $h\nu_0$ being the ionization energy of hydrogen. From equations (2) and (3) we then obtain

$$\frac{P_{\rm rad}}{P_{\rm gas}} \approx \frac{h\nu_0}{m c_0 c} = 3.3 \times 10^{-4} . \tag{4}$$

In other words, the radiation pressure acting on the base of the photoevaporated wind is completely negligible compared to the gas pressure and is thus unable to confine the photoevaporated wind.

Let us now consider the ram pressure of the wind from θ^1C Ori. Assuming that the ionizing flux is not attenuated in the photoevaporated wind, the ratio of the ram pressure to the radiation pressure can be written as

$$\frac{P_{\rm hyd}}{P_{\rm rad}} = \frac{\rho_w v_w^2}{F_0 \langle h\nu \rangle / c} = \epsilon , \tag{5}$$

where ρ_w and v_w are the density and velocity (respectively) of the wind from θ^1C Ori at the position of the proplyd, and we take F_0 equal to the stellar ionizing photon flux $F_* = \dot{S}_*/4\pi r^2$, where r is the distance to the star. For the wind parameters $\dot{M} = 4 \times 10^{-7}\ M_\odot$ yr^{-1} (mass-loss rate), $v_w = 1000$ km s^{-1}, and $\dot{S}_* = 7.24 \times 10^{48}$ s^{-1} (ionizing photon rate), which appear to be appropriate for θ^1C Ori (see § 5), $\epsilon \approx 0.6$; i.e., because this wind is radiatively driven, its ram pressure $P_{\rm hyd}$ has the same order of magnitude as the radiation pressure. In fact, as discussed in § 5, the ionizing flux F_0 that arrives at the ionization front is greatly reduced mainly by recombinations in the photoevaporated flow, i.e., $F_0 \ll F_*$. Therefore, the value of ϵ can be larger by 2 orders of magnitude, implying that the hydrodynamic pressure is dominant, clearly being the best candidate for producing a confinement of the photoevaporated wind. Moreover, while the radiation pressure acts on the base of the photoevaporated wind, the ram pressure instead acts on the surface of contact between this wind and the wind from θ^1C Ori. As the gas pressure at the base of the photoevaporated wind is so large, the surface of contact between the two winds will be spatially quite removed from the photoevaporated surface. The resulting dilution of the photoevaporated wind results in a large enough pressure drop so that it can be confined by the ram pressure of the wind from θ^1C Ori. On the other hand, a radiation pressure confinement cannot work through such a dilution of the photoevaporated wind, since the more dilute regions will be optically thin, and will not receive a substantial amount of momentum from the radiation field. In the following sections, we will explore in detail the confinement of a photoevaporated wind from a disk through the interaction with the wind from θ^1C Ori.

3. THE "CHOKED," SUBSONIC REGIME

Let us assume that we have an accretion disk around a young, low-mass star, with its axis aligned with the direction toward the exciting star (θ^1C Ori). The exciting star has two principal effects on the disk:

1. The ionizing radiation field from the exciting star photoevaporates material from the surface of the disk, and
2. The wind from the exciting star exerts a pressure on the disk that tends to confine the photoevaporated material.

The balance between these two competing processes determines the structure of the photoevaporated region surrounding the surface of the disk that faces the exciting star. This balance depends on the value of the dimensionless parameter,

$$\lambda \equiv \frac{F_0 c_0 m}{\rho_w v_w^2}, \tag{6}$$

defined as the ratio between the product of the photon flux F_0 incident on the surface of the disk times the isothermal sound speed c_0 of the ionized gas times the average mass per atom or ion m and the momentum flux of the wind from the exciting source at the position of the disk $\rho_w v_w^2$.

It is intuitively clear that for low values of λ the wind from the source will succeed in confining the material photoevaporated from the disk. This situation is shown schematically in Figure 1. In this low λ regime, the photoevaporated material leaves the surface of the disk with a density ρ_0 and a subsonic velocity $v_d < c_0$. A fully subsonic bubble of photoionized material is formed, limited on one

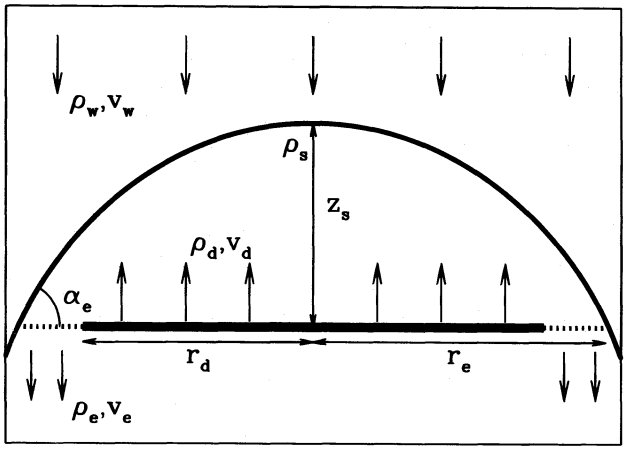

FIG. 1.—Confinement of the photoevaporated wind in the low λ regime. The fast wind from θ^1C Ori confines the ionized disk material to a subsonic bubble. Symbols are defined in the text.

side by the surface of the disk (which is facing the exciting source) and on the other side by the curved contact discontinuity that separates the photoevaporated bubble from the incident wind. Since the adiabatic expansion is negligible, this confined bubble is isothermal at a temperature of $\approx 10^4$ K.

The material trapped in the bubble can only escape downwind (away from the θ^1C Ori) in the unbounded region beyond the outer edge of the disk. In order to allow this escape of mass, the bubble has to have a radius (on the equatorial plane of the disk) $r_e > r_d$, where r_d is the radius of the accretion disk. As the bubble is subsonic, the material that starts to escape freely into the unconfined region downwind from the disk will immediately go through a sonic transition. We can therefore assume that the material leaves the bubble with a velocity $v_e \approx c_0$.

Further progress can be made by assuming that the flow is in a steady state, in which every photon that impinges on the disk results in an ion being photoevaporated from the disk and eventually leaving the bubble through the region of exit (see Fig. 1). In other words,

$$\pi r_d^2 m F_0 = \pi r_d^2 \rho_d v_d = \pi (r_e^2 - r_d^2) \rho_e v_e , \tag{7}$$

where ρ_e is the exit density (assumed to be uniform across the exit region, see Fig. 1), and $v_e \approx c_0$. We have assumed that both ρ_d and v_d are constant over the whole surface of the accretion disk.

Let us also consider the on-axis stagnation point between the photoevaporated material and the wind from the exciting source. At this point, the material in the bubble has zero velocity, and a density ρ_s (see Fig. 1). The stagnation pressure is also approximately equal to the ram pressure of the impinging wind, so that we have

$$\rho_s c_0^2 \approx \rho_w v_w^2 . \tag{8}$$

Finally, we can use Bernoulli's theorem for the stagnation streamline, which relates the exit conditions (ρ_e and v_e), the stagnation point conditions (ρ_s, $v = 0$), and the velocity and density (ρ_d and v_d) of the gas that is photoevaporated from the central regions of the accretion disk. Neglecting gravity, an issue that we will return to in § 5, the isothermal Bernoulli's theorem then gives

$$\frac{c_0^2}{2} + c_0^2 \ln \rho_e = c_0^2 \ln \rho_s = \frac{v_d^2}{2} + c_0^2 \ln \rho_d , \tag{9}$$

where we have set $v_e = c_0$.

We can then calculate the value of the outer radius r_e of the bubble (see Fig. 1) by combining equations (7)–(9) to obtain

$$r_e = (1 + \lambda e^{1/2})^{1/2} r_d , \tag{10}$$

where the dimensionless parameter λ has been defined by equation (6).

From this equation, it is clear that for larger values of λ, the photoevaporated bubble grows in size. However, there is a limit in the value of λ allowed in this model, so that $r_e \sim r_d$. In order to see this, one can use equations (7)–(9) to obtain an implicit equation:

$$\lambda = M_d e^{-M_d^2/2} , \tag{11}$$

which gives the Mach number $M_d = v_d/c_0$ of the material leaving the surface of the disk as an implicit function of the dimensionless parameter λ. This equation implies that

$$\lambda \leq \lambda_m \equiv e^{-1/2} \tag{12}$$

and that the maximum value of λ is obtained for a sonic, $M_d = 1$ situation. Note that the solutions with $M_d > 1$ are unphysical, because in our derivation we have assumed that we have a fully subsonic, causally connected bubble. From equations (10) and (12) we also see that the radius of the bubble (measured along the plane of the disk) is limited to values $r_e \leq 2^{1/2} r_d$.

It is possible to estimate the angle α_e (see Fig. 1) of the surface of the bubble as it intersects the equatorial plane of the disk by setting the exit pressure $\rho_e c_0^2$ equal to the ram pressure of the environment normal to the surface:

$$\rho_e c_0^2 \approx \rho_w v_w^2 \cos^2 \alpha_e . \tag{13}$$

Combining this equation with equations (8) and (9), we obtain that $\cos \alpha_e = e^{-1/4}$, or $\alpha_e = 38.^\circ 85$. A crude estimate of the shape of the subsonic bubble is obtained by assuming that it has a quadratic shape of the form

$$\frac{z}{r_e} = 0.403 \left[1 - \left(\frac{r}{r_e} \right)^2 \right] , \tag{14}$$

which gives the height z of the bubble (above the equatorial plane of the disk) as a function of the cylindrical radius r. The value of $0.403 = (\tan \alpha_e)/2$ has been chosen so that the assumed shape has the correct slope on intersection with the equatorial plane of the disk. This assumed shape implies a bubble size $z_s = 0.403[1 + \lambda e^{1/2}]^{1/2} r_d$ measured along the symmetry axis (see Fig. 1). Then, this bubble has an aspect ratio of $\sim 1/2$ since z_s/r_d is always less than 0.6.

4. THE "FREE," SUPERSONIC REGIME

4.1. *The Disk Wind*

Let us now assume that the dimensionless parameter λ (defined by eq. [6]) has a value $\lambda > \lambda_m$ (see eq. [12]). Under this condition, the ram pressure of the impinging wind is not strong enough to confine the photoevaporated wind in a subsonic bubble. Instead, the photoevaporated wind will be able to expand supersonically. In this section, we will derive an approximate analytic description of this freely expanding wind.

We will assume that the photoevaporated material enters into an expansion fan (Courant & Friedrichs 1948) and leaves the disk with a sonic velocity along the sym-

metry axis,

$$v_z(0, r) = c_0 , \tag{15}$$

and a velocity parallel to the surface of the disk,

$$v_r(0, r) = \left(\frac{r}{r_d}\right) c_0 , \tag{16}$$

which is a linear function of the cylindrical radius r and becomes sonic at the outer radius r_d of the disk (see Fig. 2).

We will furthermore assume that the streamlines of the photoevaporated wind are straight, so that they are given by

$$r = r_0(1 + z/r_d) , \tag{17}$$

where r_0 is the cylindrical radius at which the streamline crosses the disk, and we have used equations (15) and (16). From equation (17) it is clear that our wind solution is confined to a cone with a half-opening angle of 45°.

The isothermal Bernoulli's theorem along a streamline can be written as

$$v_z = c_0 \left[1 + 2 \cos^2 \alpha \ln\left(\frac{\rho_0}{\rho}\right)\right]^{1/2} , \tag{18}$$

where ρ_0 is the density at the position of the disk, and α is the angle between the streamline and the symmetry axis (see Fig. 2). Note that we are again neglecting gravity.

Also, from the usual mass conservation argument, it is straightforward to show that the density has to obey the relation

$$\rho = \frac{\rho_0 c_0}{v_z} \frac{r_d^2}{(r_d + z)^2} , \tag{19}$$

where we have used equation (17).

Equations (18) and (19) can then be combined to give an implicit equation for the density of the wind:

$$\rho = \frac{\rho_0 r_d^2}{(r_d + z)^2} \left[1 + 2 \cos^2 \alpha \ln\left(\frac{\rho_0}{\rho}\right)\right]^{-1/2} . \tag{20}$$

This equation can be solved for ρ in an approximate way by first neglecting the logarithmic term in equation (20) to obtain a first approximation,

$$\rho^{(a)} \approx \frac{\rho_0 r_d^2}{(r_d + z)^2} , \tag{21}$$

which can be then inserted into the logarithmic term of equation (20) to obtain the better approximation:

$$\rho \approx \frac{\rho_0 r_d^2}{(r_d + z)^2} \left\{1 + 2 \cos^2 \alpha \ln\left[\frac{(r_d + z)^2}{r_d^2}\right]\right\}^{-1/2} . \tag{22}$$

In the following, we will always use this approximate, explicit form for the density of the photoevaporated wind.

Finally, equations (18) and (22) can be combined to give the ram pressure of the photoevaporated wind, in the direction of the streamlines, at large distances from the disk:

$$\rho v^2 = \rho_0 c_0^2 \left(\frac{r_d}{R}\right)^2 \frac{1}{\cos^4 \alpha} \left[1 + 4 \cos^2 \alpha \ln\left(\frac{r}{r_d} \frac{1}{\tan \alpha}\right)\right]^{1/2} , \tag{23}$$

where we have considered that for $z \gg r_d$, the spherical radius R is given by $R = z/\cos \alpha$ and we have substituted equation (21) into the logarithmic term of equation (18).[1] In the following section, we will use this ram pressure to calculate the shape of the interface between the photoevaporated wind and the wind from θ^1C Ori.

4.2. *The Mach Disk*

We will assume that the shape of the interface between the photoevaporated wind and the wind from θ^1C Ori is determined by the ram pressure balance between the two winds (in other words, we will neglect the centrifugal and Coriolis pressures). Let us consider the interaction between a plane parallel wind of density ρ_w and velocity v_w with a radially diverging wind of position-dependent density ρ and velocity v.

The condition of ram pressure balance between these two winds can be written as

$$\rho v^2 \cos^2 \theta' = \rho_w v_w^2 \cos^2 (\theta - \theta') , \tag{24}$$

where the angles θ and θ' are defined in Figure 3. In terms of the cylindrical radius $r = R \sin \theta$, the ram pressure balance equation takes the simple form

$$\frac{dr}{d\theta} = r_d \psi , \tag{25}$$

where

$$\psi = \left(\frac{\rho}{\rho_w}\right)^{1/2} \frac{v}{v_w} \frac{R}{r_d} \tag{26}$$

and r_d is a characteristic radius (in our case, the radius of the accretion disk) used to obtain a dimensionless form for ψ. We should note that if we set $\psi = 1$ (i.e., for the case of a spherically symmetric constant velocity photoevaporated wind), we obtain $r = r_d \theta$, which is the well-known solution found by Dyson (1976).

If we consider the plane that contains the axis of the disk and the direction to θ^1C Ori, at large distances from the disk (i.e., for $R \gg r_d$) the angles θ and α (see Figs. 2 and 3) are

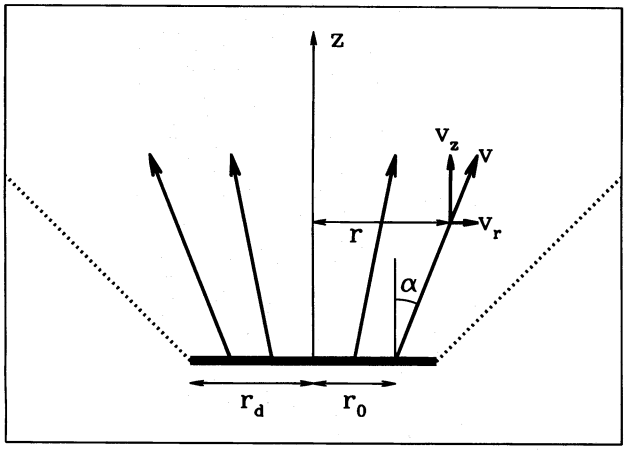

FIG. 2.—Streamlines of the photoevaporated wind in the high λ regime. Ionized disk material freely expands in a Mach cone of opening half-angle 45°.

[1] In the above equation, cylindrical and spherical coordinates are mixed for convenience (see § 4.2).

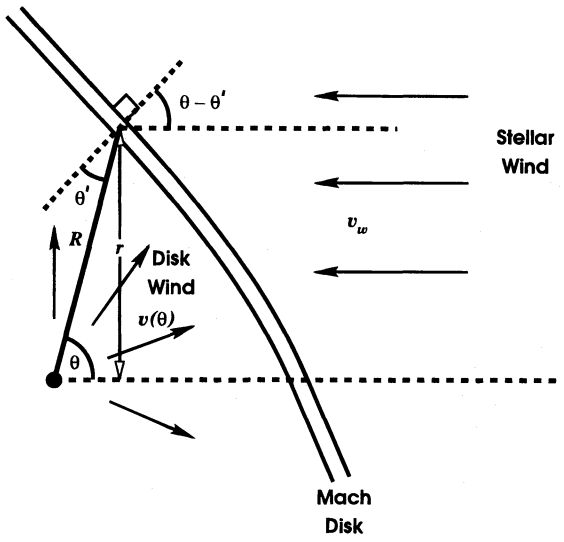

FIG. 3.—Ram pressure balance between the photoevaporated wind and the wind from θ^1C Ori.

related through $\alpha = \theta_0 - \theta$, where θ_0 is the angle between the disk axis and the direction to θ^1C Ori. For this plane, equation (26) can then be written as

$$\psi = \frac{\lambda^{1/2}}{\cos^2(\theta_0 - \theta)} \times \left\{1 + 4\cos^2(\theta_0 - \theta)\ln\left[\frac{r}{r_d}\frac{1}{\tan(\theta_0 - \theta)}\right]\right\}^{1/4}, \quad (27)$$

where

$$\lambda = \frac{\rho_0 c_0^2}{\rho_w v_w^2} = \frac{F_0 m c_0}{\rho_w v_w^2} \quad (28)$$

and we have used equation (23). The second equality of equation (28) is obtained by assuming that the density at the beginning of the expansion fan is the same as that of the ionization front (small divergence) and that the ionization front is D-critical, i.e., the material is released at the sonic speed.

It is possible to solve equation (25) (with the value of ψ given by eq. [27]) with a method of successive approximations. The first approximation is obtained by setting the term in braces in (27) equal to 1. Equation (25) can then be integrated in a straightforward way to give

$$r^{(a)}(\theta) = \frac{\lambda^{1/2} r_d}{\cos^2\theta_0}\left[\frac{\tan\theta}{1 + \tan\theta_0\tan\theta}\right], \quad (29)$$

which is the equation for a straight line parallel to the surface of the accretion disk, at a distance $z = r/\tan(\theta) = \lambda^{1/2} r_d/\cos^2\theta_0$ from the disk. From this result, it is clear that our approximation of large distances from the accretion disk (under which eq. [23] was derived) is valid provided that $\lambda \gg 1$.

The next approximation to the locus of the surface of ram pressure balance can be obtained by substituting $r^{(a)}$ (eq. [29]) into the right-hand side of equation (27) and considering that the terms inside the braces are dominated by the term in $\ln\lambda$, as we are considering the $\lambda \gg 1$ regime (see above). In order to integrate equation (25) we assume that the solution has the form $r(\theta) = p(\theta) r^{(a)}(\theta)$, where $p(\theta)$ is a polynomial of degree n in θ. We then find

$$r(\theta) = \frac{2^{1/4}\lambda^{1/2}(\ln\lambda)^{1/4} r_d \tan\theta}{\cos^2\theta_0(1 + \tan\theta_0\tan\theta)} \times \left[1 - \frac{1}{4}\left(\theta_0^2 + \frac{\theta^2}{3} - \theta_0\theta\right)\right], \quad (30)$$

where we have considered the solution to order $n = 2$ in the polynomial $p(\theta)$. This solution is plotted in Figure 4 for different values of the orientation θ_0 between the disk axis and the direction to θ^1C Ori. From this graph it is clear that the shape of the ram pressure balance surface is approximately straight, since the term in brackets in equation (30) is only a small correction. This justifies our neglect of centrifugal and Coriolis forces.

It can easily be shown that off the plane containing the disk axis and the direction to θ^1C Ori, the curvature of the ram pressure balance surface is also small. Therefore, the shocked region between the photoevaporated wind and the wind from θ^1C Ori is approximately planar and parallel to the surface of the disk and lies at a distance

$$D \approx \frac{2^{1/4}\lambda^{1/2}(\ln\lambda)^{1/4} r_d}{\cos^2\theta_0}, \quad (31)$$

from the accretion disk (see eq. [30]).

4.3. *The Flow along the Mach Disk*

Let us now assume that the ram pressure balance surface is given by the planar solution described in the previous section. As is shown in Figure 5, this planar surface is limited radially by the 45° half-opening angle cone to which the photoevaporated wind is circumscribed (see § 4.1). In this way, the shock in the photoevaporated wind can be described as a planar "Mach disk."

In this section, we will consider the postshock flow (of the photoevaporated wind), which moves away from the z-axis along this Mach disk. From equations (18) and (22) it is possible to determine the density and the spatial velocity

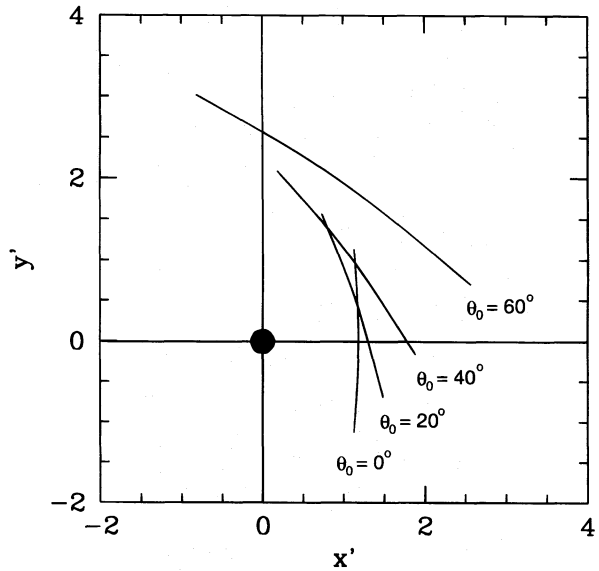

FIG. 4.—Shape of the Mach disk for different values of the inclination angle θ_0 between the normal to cicumstellar disk and the direction to θ^1C Ori. Values of θ_0 of 0°, 20°, 40°, and 60° are shown. It can be seen that the Mach disk is nearly flat in each case. The coordinates x' and y' are in units of $\lambda^{1/2}(2\ln\lambda)^{1/4} r_d$, see eq. (30).

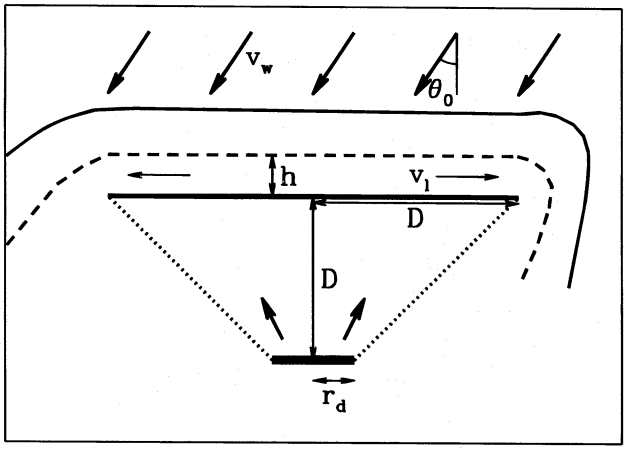

FIG. 5.—Gas flow in the Mach disk, illustrating the quantities that enter into eqs. (32)–(34).

just upstream of the Mach disk. Through the usual mass and momentum conservation equations, and noting that the pressure of the postshock gas has to be equal to the normal ram pressure $\rho_w v_w^2 \cos^2 \theta_0$ of the wind from θ^1C Ori, one can show that in the $\lambda \gg 1$ regime the outward velocity v_l along the Mach disk (see Fig. 5) is given by

$$v_l = \frac{2^{7/2}(\ln \lambda)^{1/2}}{3} \left(\frac{r}{D}\right) c_0 , \tag{32}$$

where the distance D between the accretion disk and the Mach disk is given by equation (31). The width h of the shocked photoevaporated wind layer (see Fig. 5) is found to have a value

$$h = \frac{3}{8 \ln \lambda} D , \tag{33}$$

which is independent of the cylindrical radius r. The density of the shocked layer ρ_l is also independent of r and can be found from the pressure balance condition to be

$$\rho_l = \frac{\rho_w v_w^2 \cos^2 \theta_0}{c_0^2} . \tag{34}$$

From equation (33), we see that for large λ the shocked layer has a width $h \ll D$ (i.e., the layer is thin). Also, from equation (32) we see that at the edge of the Mach disk (i.e., for $r = D$) the radial velocity of the shocked material is highly supersonic. In this model, a thin sheet of material is thrown off the edge of the Mach disk at a supersonic velocity.

This radially expanding sheet of material does not have support from the photoevaporated wind (which is confined to a 45° opening angle cone; see § 4.1), but it clearly continues to interact with the wind from θ^1C Ori (see Fig. 5). The resulting effect is that this flow has to curve backward and eventually become approximately parallel to the direction pointing away from θ^1C Ori. This curving flow is described in detail in the following section.

4.4. *The Bow Shock Wings*

From equation (32), we see that the flow leaving the edge of the Mach disk has an initial velocity

$$v_0 = v_l(r = D) = \frac{2^{7/2}(\ln \lambda)^{1/2}}{3} c_0 . \tag{35}$$

Also, from simple geometrical arguments one sees that the initial angle δ_0 of this flow with respect to the direction pointing away from θ^1C Ori is given by

$$\tan \delta_0 = \frac{(1 - \sin^2 \phi \sin^2 \theta_0)^{1/2}}{\sin \phi \sin \theta_0} , \tag{36}$$

where ϕ is the azimuthal angle measured around the axis pointing from the disk to θ^1C Ori (with $\phi = 0$ corresponding to the plane containing v_w and the disk axis).

Figure 6 shows a schematic diagram of the flow leaving the edge of the Mach disk. It is possible to obtain the curved path of this flow from Newton's second law,

$$\rho h a = \rho_w v_w^2 \sin^2 \delta , \tag{37}$$

where ρ is the density, h is the initial width of the curved sheet, and the acceleration a of the material is given by

$$a = v_0^2 \kappa ,$$
$$\kappa = \frac{d^2x/dy^2}{[1 + (dx/dy)^2]^{3/2}} , \tag{38}$$

with κ being the curvature of the path. In deriving equation (38), we have considered that the tangential forces along the curved path are small (because the flow is highly supersonic), so that the tangential velocity remains constant (with a value equal to v_0, see eq. [35]). The x- and y-coordinates describing the path of the flow are defined in Figure 6.

We will now assume that the path of the material ejected from the edge of the Mach disk curves over a distance that is much smaller than the radius D of the Mach disk. Under this approximation, the flow can be treated with a plane-parallel approximation, under which the product $\rho h v_0$ will be constant along the curved sheet. Equations (37) and (38), then, give

$$\frac{d^2x'}{dy'^2} = \frac{1}{L}\left[1 + \left(\frac{dx'}{dy'}\right)^2\right]^{1/2} , \tag{39}$$

where we have defined dimensionless coordinates $y' = y/D$ and $x' = x/D$, and the characteristic length L is given by

$$L = \frac{\rho v_0^2}{\rho_w v_w^2} \frac{h}{D} = \frac{1}{12} . \tag{40}$$

The somewhat surprising result shown in the second equality is obtained by substituting the appropriate values from equations (31) and (35). The fact that this characteristic length is 1/12 of the radius of the Mach disk clearly justifies the plane-parallel assumption made for deriving equation

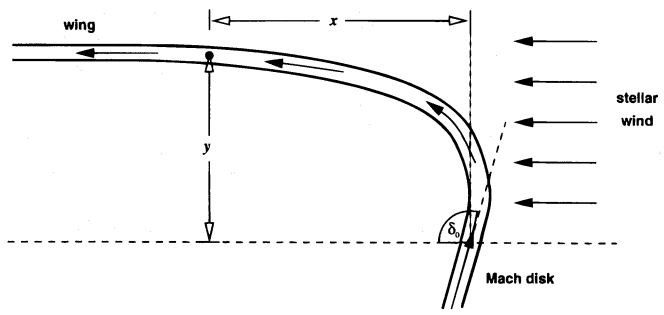

FIG. 6.—Gas flow leaving the edge of the Mach disk. The initial injection angle with respect to the fast wind direction is δ_0. The coordinates x and y, used in describing the subsequent motion of the gas (eqs. [37] and [38]), are indicated.

(39). This equation can then be integrated in a straightforward way to obtain

$$x' = L\left\{\cosh\left[\frac{y}{L} - \sinh^{-1}\left(\frac{1}{\tan\delta_0}\right)\right] - \frac{1}{\sin\delta_0}\right\}. \quad (41)$$

In this way, we have derived a full description of the flow resulting from the interaction of the wind from θ^1C Ori and the material ejected from the edges of the Mach disk. Even though the geometry of the problem is somewhat complicated, from equations (36), (40), and (41) it is possible to construct the three-dimensional surface composed by the Mach disk and by the "bow shock wings" formed by the material ejected sideways from this disk.

Examples of such surfaces are shown in Figure 7 for different values of the angle θ_0 between the disk axis and the direction to θ^1C Ori. From this figure, we see that the picture developed in §§ 4.1–4.4 is actually valid only for values of θ_0 not larger than $\approx 60°$. For larger values of θ_0, the "bow shock wing" will start to intersect the photoevaporated wind cone, giving rise to a pattern of sideways shocks, which we have not attempted to explore.

Finally, we should note that in the high-λ regime most of the physical parameters of the model enter only through a scaling of the radius D of the Mach disk. Moreover, the shape of the shocked surface written in units of D depends only on the orientation angle θ_0 between the disk axis and the direction to θ^1C Ori.

5. THE VALUE OF THE DIMENSIONLESS PARAMETER λ

In order to calculate the dimensionless parameter λ (eq. [6]) one needs to know the incident photon flux at the ionization front F_0 and the stellar wind parameters of the exciting star $\dot{M}_w$ and v_w. We obtain the former following Pastor, Cantó, & Rodríguez (1991), who included the effect of dust absorption of the ionizing photons in the photoevaporated flow, and write

$$F_0 = F_* e^{-(\tau_w + \tau_0)} - f(\tau_0) n_0^2 \alpha_B r_d , \quad (42)$$

where F_0 ($\equiv n_0 c_0$) is the flux of ionizing photons that arrive at the D-critical ionization front. The first term on the right-hand side of equation (42) represents the flux of ionizing photons from the exciting star ($F_* \equiv \dot{S}_*/4\pi r^2$) after attenuation by dust in the star's stellar wind and in the photoevaporated disk wind itself, with dust extinction optical depths of τ_w and τ_0 respectively. For the density distribution of our photoevaporated wind (eq. [22]), and assuming $\theta_0 =$

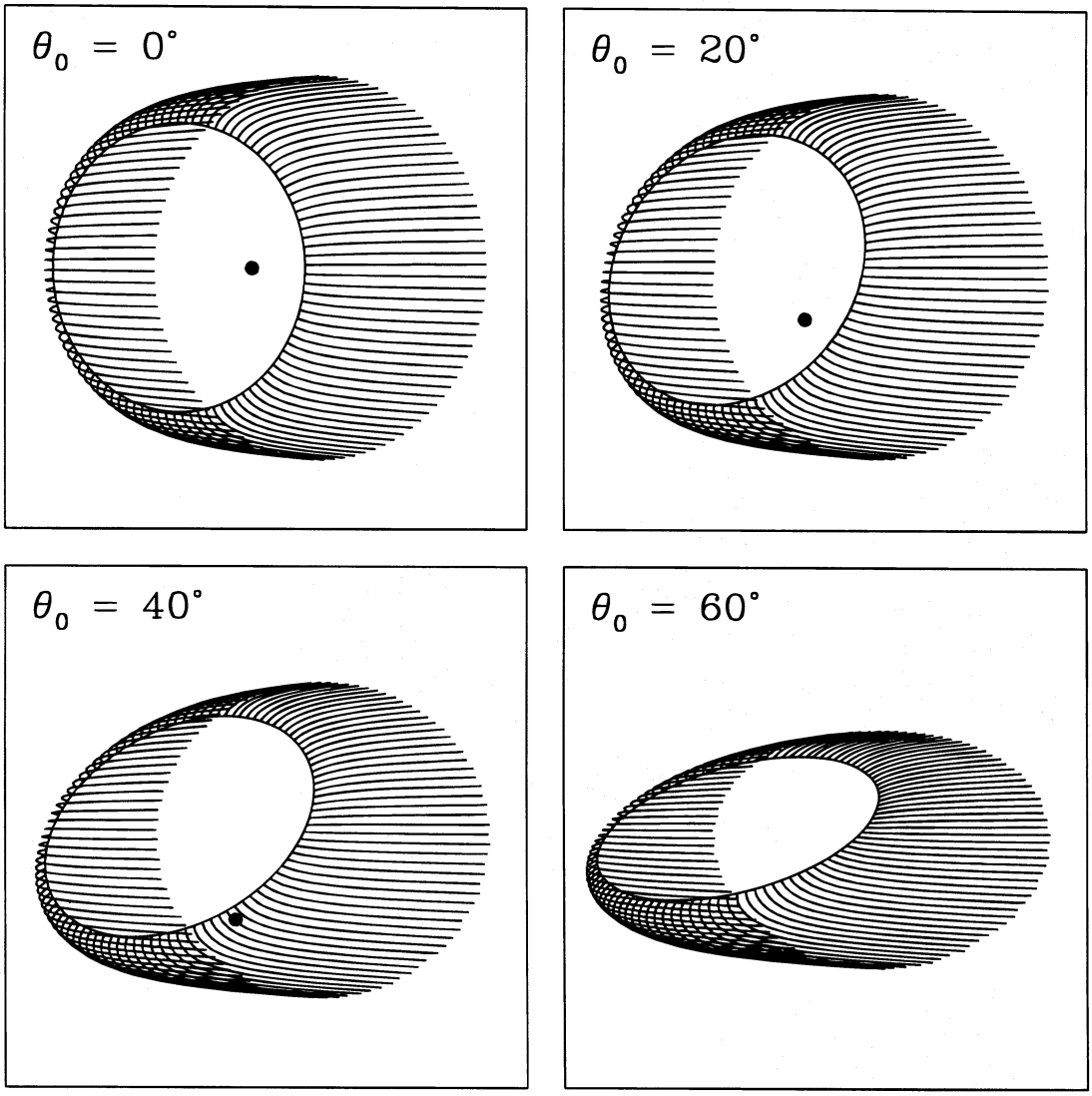

FIG. 7.—Shape of the bow shock wings for various angles θ_0 between the disk normal and the direction to θ^1C Ori

0, one can write $\tau_0 \simeq \sigma_d n_0 r_d$, where σ_d is the dust extinction cross section per hydrogen atom in the Lyman continuum (assumed to be 2.0×10^{-21} cm^2). In this approximation, we make no distinction between true absorption and scattering.

The second term on the right-hand side of equation (42) represents those photons lost through ionization of the gas in the photoevaporated wind, which in equilibrium must balance the recombinations in this wind. Here, $\alpha_B = 2.6 \times 10^{-13}$ cm^3 s^{-1} is the Case B recombination rate and $f(\tau_0)$ is a factor that takes into account the variation in both the gas density and the dust optical depth with height in the photoevaporated wind. Unlike in the case considered by Pastor et al. (1991),whose $b(\tau_d^0)\exp(-\tau_d^0)$ corresponds to our $f(\tau_0)$, we can find an analytic expression for this factor under the reasonable approximation that the vast majority of the recombinations occur in the base of the wind, before the gas has undergone significant acceleration. In this case, we find $f(\tau_0) = \tau_0^{-3}\{\tau_0^2 - 2\tau_0 + 2[1 - \exp(-\tau_0)]\}$, which can be further crudely approximated as $f(\tau_0) \simeq (3 + \tau_0)^{-1}$. This latter approximation is exact in the limits $\tau_0 = 0$ and $\tau_0 \to \infty$, with a maximum error of less than 10%.

Figure 8 (*upper panel*) shows the resulting dust optical depth as a function of distance of the proplyd from the exciting star θ^1C Ori, which is assumed to be of spectral type O7 V (Conti 1973) with an ionizing photon rate $\dot{S}_* = 7.24 \times 10^{48}$ s^{-1} (Panagia 1973) and with $\tau_w = 0$. The photoevaporated disk is assumed to have a radius of $r_d = 15$ a.u. The vertical dotted lines in the figure indicate the rough limits of the observed distances of the proplyds from θ^1C Ori (0.01–0.2 pc). It can be seen that the dust extinction in the photoevaporated wind is only important for proplyds quite close to the exciting star (<0.05 pc). Dust in the wind of θ^1C Ori itself ($\tau_w \neq 0$) cannot be ruled out a priori, and its likely effect on λ will be discussed further below.

The center panel of Figure 8 shows the logarithm of the density of the gas leaving the ionization front at the base of the photoevaporated wind. The solid line is calculated from equation (42) and includes the effects of dust, whereas the dashed line shows the density that would obtain in the absence of dust ($\tau_0 = 0$). Since, for the parameters considered here, one finds that $F_0 \ll F_*$, the density in the dust-free case is given to a very good approximation by $n_0 \simeq [3\dot{S}_*/(4\pi\alpha_B r_d)]^{1/2} r^{-1}$.

For the wind parameters of θ^1C Ori, we use $\dot{M}_w = 4 \times 10^{-7}\, M_\odot$ yr^{-1}, $v_w = 1000$ km s^{-1}, obtained by Howarth & Prinja (1989) from measurements of UV resonance lines. Although this seems to be the most reliable estimate, it is in conflict with the Hα measurements of Leitherer (1988), which imply a stronger wind ($\dot{M}_w = 7.5 \times 10^{-7}\, M_\odot$ yr^{-1}, $v_w = 1650$ km s^{-1}). Also, both these estimates give a $\dot{M}_w/v_w$ ratio that is a factor of 2 lower than the one implied by equation (24) of Panagia & Felli (1975) given the detected free-free emission of 0.49 mJy at 3.5 cm (Menten & Reid 1996). Thus, we note that the uncertainty in the momentum flux of the stellar wind means that λ could be a factor of ~ 3 less than we have assumed.

The resultant value of λ as a function of distance from θ^1C Ori is shown in the lower panel of Figure 8. The solid line is with dust and the dashed line is without dust. In the dust-free case, λ varies approximately linearly with distance as $\lambda \simeq 50(r/0.01\ \text{pc})$. The effect of dust is to decrease λ, with the maximum reduction being by about a factor of 2 and occurring for the proplyds closest to θ^1C Ori. One can see that, for the parameters of θ^1C Ori, $\lambda \gg 1$, and the model discussed in § 4 applies. In this model, the radius of the Mach disk is given by D in equation (31). Figure 9 shows as a solid line the value of D as a function of the distance to θ^1C Ori in arcsec for disk sizes $r_d = 20$ a.u. and $\theta_0 = 0$. The filled triangles correspond to the proplyd sizes measured at

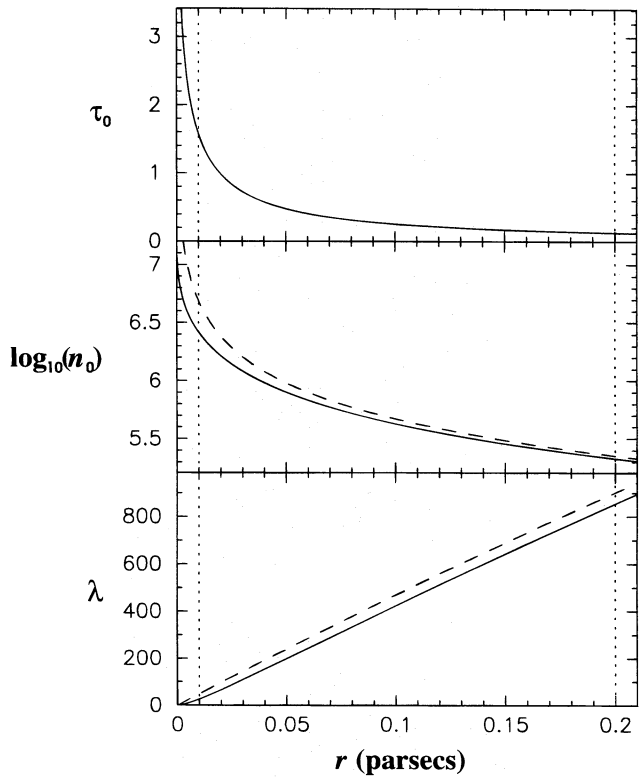

FIG. 8.—Dust optical depth (*upper panel*), logarithmic gas density at the ionization front (*center panel*), and the parameter λ (*lower panel*) as functions of distance from the proplyd to θ^1C Ori. Dashed lines indicate the dust-free case ($\tau_0 = 0$). Vertical dotted lines delineate the range of distances at which the proplyds are found.

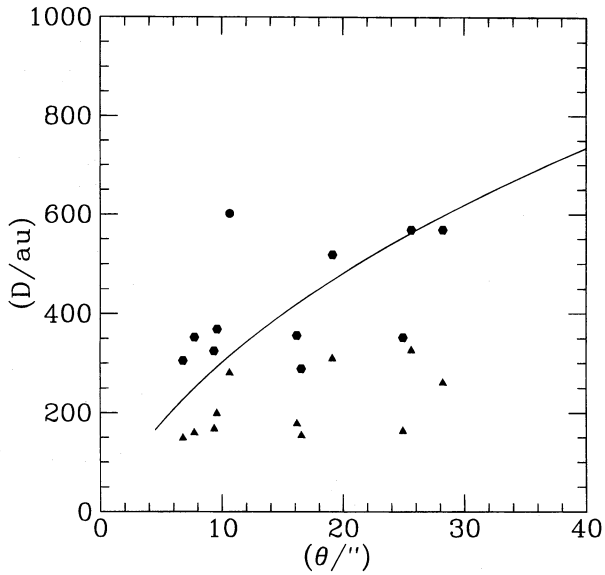

FIG. 9.—Proplyd size D as a function of distance to θ^1C Ori. Solid line shows model prediction for $r_d = 20$ a.u. Filled symbols are measured from *HST* images at the 50% contour (*triangles*) and 10% contour (*hexagons*).

the 50% intensity contour (FWHM) directly from the Hα images of O'Dell & Wen (1994). These FWHM sizes are smaller than D because the photoevaporated winds (and possible the central stars) are much brighter than the Mach disk. Therefore, we also show, by filled hexagons, the sizes of the proplyds measured perpendicular to the direction to θ^1C Ori at the contour corresponding to 10% of the peak intensity. This should be a truer measure of D and indeed can be seen to be in reasonable agreement with the theoretical prediction. No correction has been made for projection effects in this or in the following graph, so, assuming an isotropic distribution of proplyds with respect to θ^1C Ori, the real distances will be on average (median) 15% larger than indicated.

The values of λ calculated in this section and shown in Figure 8 could be overestimates for two reasons. First, there is the possible extinction due to dust in the wind of θ^1C Ori. There exists some evidence for the existence of grains in the wind-swept cavity around θ^1C Ori from scattering studies in the ultraviolet (Patriarchi & Perinotto 1985) and optical (Leroy & Le Borgne 1987). The total line-of-sight extinction to θ^1C Ori is $E(B-V) = 0.32$ mag (Bohlin & Savage 1981), which, based on the Orion extinction curve (Cardelli & Clayton 1988), implies an optical depth in the Lyman continuum of $\tau_{\rm EUV} \simeq 3$. However, the dust-gas ratio in the cavity around θ^1C Ori is much reduced (Mathis et al. 1981), consistent with most of the extinction occurring in a foreground screen, possibly the neutral lid (as suggested by O'Dell, Walter & Dufour 1992, based on a comparison of Hβ and 21 cm maps of the nebula). It would therefore be surprising if the Lyman optical depth between θ^1C Ori and the proplyds were much larger than unity, so the reduction in λ due to this mechanism should not be by more than a factor of 2. In fact, in the absence of mass loading of the stellar wind (see § 8), the effect must be even smaller than this. Even assuming a normal dust-to-gas ratio outside the dust destruction radius r_0 (assumed to be where the equilibrium dust temperature exceeds 2000 K), one finds for a wind of constant mass flux and with parameters appropriate to θ^1C Ori that the dust optical depth through the wind in the Lyman continuum is only $\tau_w \simeq 0.06$.

Second, the model developed in § 4 neglects gravity, which is only valid for those parts of the circumstellar disk where the sound speed greatly exceeds the local escape speed. The critical radius at which these speeds are equal can be calculated to be $r_c = 17.8 M_*$ a.u., where M_* is the mass of the central star in solar masses. As will be seen in § 7, r_c is not much smaller than the disk radii r_d derived from our model fits. However, the effects of gravitational deceleration can be roughly accounted for in a simple-minded fashion by using an effective area for the base of the disk wind, equal to $\pi(r_d^2 - r_c^2)$, rather than the full area of the disk. This will lead to a reduction of λ by a factor of $\phi = 1 - (r_c/r_d)^2$. For the model fits of § 7, ϕ has a typical value of 0.5, so we conclude that the combined effects of the gravitational deceleration and the extinction in the wind of θ^1C Ori may reduce λ to as little as 5 for the proplyds that lie closest to θ^1C Ori. Even in such a case, we expect the high-λ calculation of § 7 to be the appropriate one.

Finally, Figure 10 shows as solid hexagons the Hα luminosity of the proplyds in units of the solar luminosity versus the distance to θ^1C Ori in arcsec taken from Table 1 of McCullough et al. (1995). The solid lines show the luminosity of proplyds models including the contribution from the photoevaporated wind for different disk sizes ($r_d = 20$ a.u. and $r_d = 60$ a.u., respectively). The dashed lines correspond to the emission of the photoevaporated winds alone. As will be shown in the next section, the photoevaporated winds are the most luminous part of our models. From this graph one can see that the observed luminosities of the proplyds can be accounted for by photoevaporated winds from disks with radii in the range 20 a.u. $< r_d <$ 60 a.u.

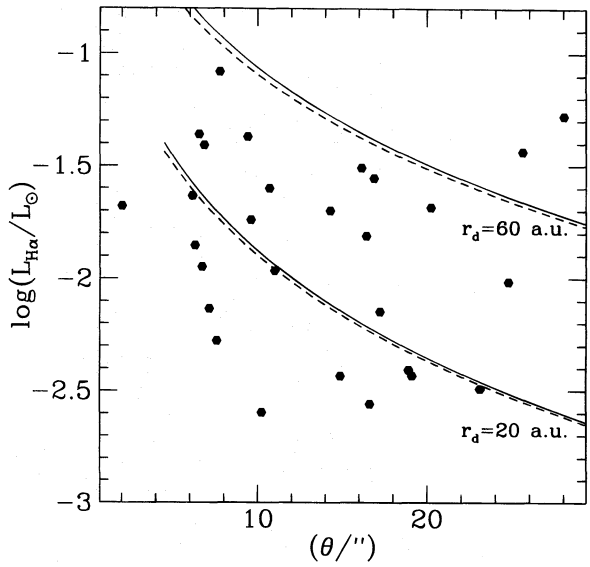

FIG. 10.—Dependence on distance to θ^1C Ori of the Hα luminosity of the proplyds measured by McCullough et al. (1995) is compared to our model predictions for two different sizes.

6. MODEL PREDICTIONS FOR EMISSION-LINE IMAGES

In calculating the emission of our models, we assume that the photoevaporated wind, Mach disk, and bow-shock wings are all isothermal at a temperature of $\sim 10^4$ K. This is a reasonable assumption, since the thermal balance of the gas will be totally dominated by the photoionizing radiation field of θ^1C Ori and it can be shown that the energy input from the wind of θ^1C Ori can only make a negligible contribution to the proplyd luminosities. Hence, the emissivity in a given line is only proportional to the square of the electron density, and hence to ρ^2, since the gas is always fully ionized. With the further assumption that the emission is always optically thin, images in a given line (say Hα) just reflect the distribution of the emission measure $\int n_e^2\, dl$.

The relative contributions of the three components of the flow are now considered. By integrating the emissivity over the emitting volume of the photoevaporated wind and of the Mach disk, one finds that the ratio of the luminosities of these two components is given by

$$\frac{L_{\rm p}}{L_{\rm m}} = \frac{4D}{3r_d} \simeq \frac{1.59}{\cos\theta_0}\,\lambda^{1/2}(\log\lambda)^{1/4}\,. \qquad (43)$$

Since, according to the previous section, appropriate values of λ are of order 30, this ratio should be quite large, of order 10. This calculation has ignored the occultation of the base of the wind by the circumstellar disk, which will occur whenever the vector from the proplyd to θ^1C Ori is directed away from the observer. However, due to the divergence of

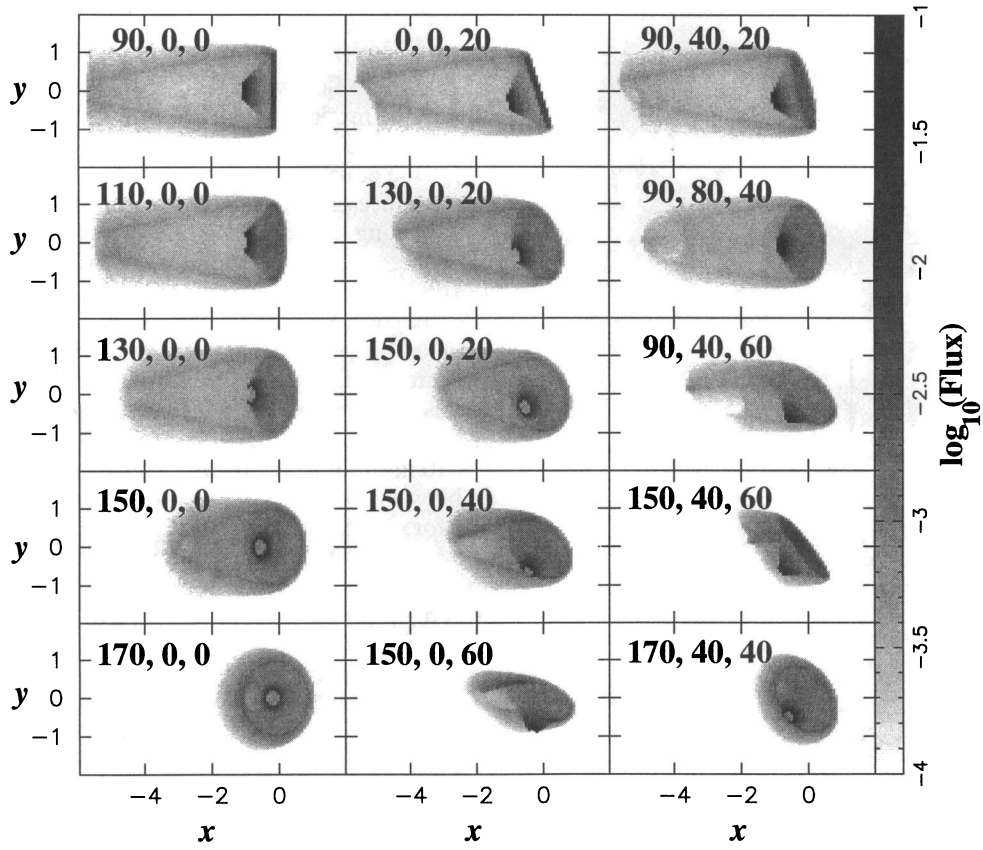

FIG. 11.—Raw emission-line images of our models with $\lambda = 10$. Each image is labeled with the value of α, β, and θ_0 (see Fig. 13). The flux scale (in arbitrary units) is shown on the right.

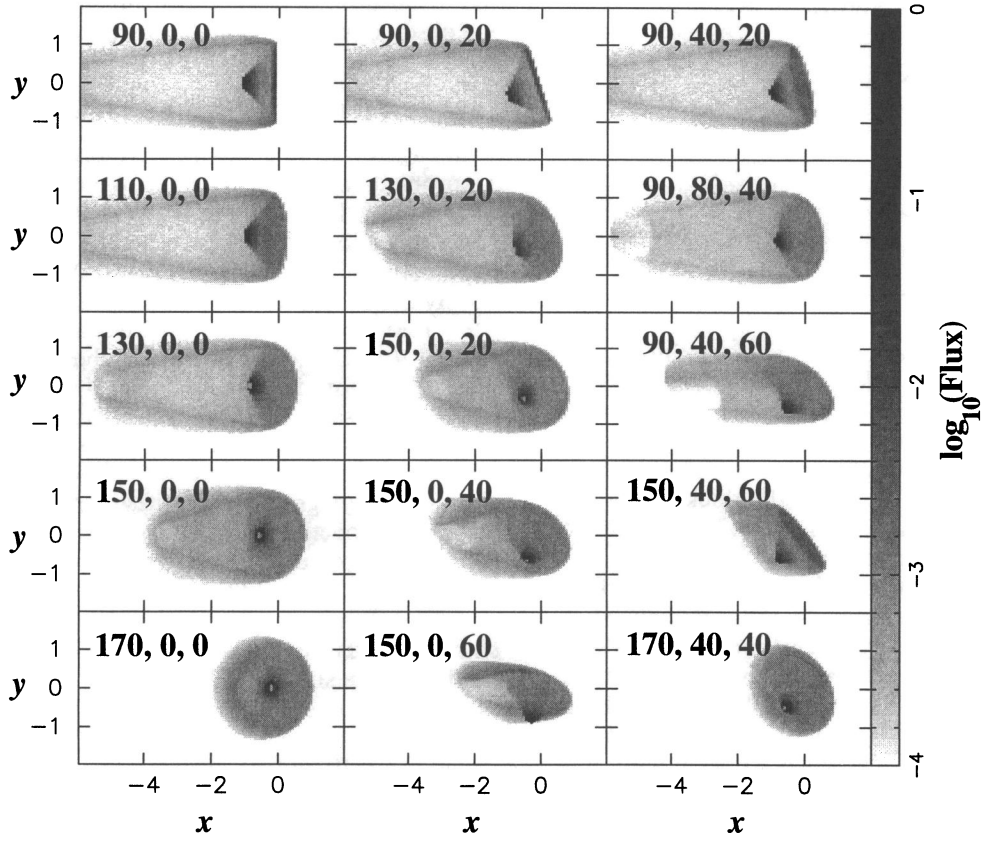

FIG. 12.—Same as Fig. 11, but for $\lambda = 30$

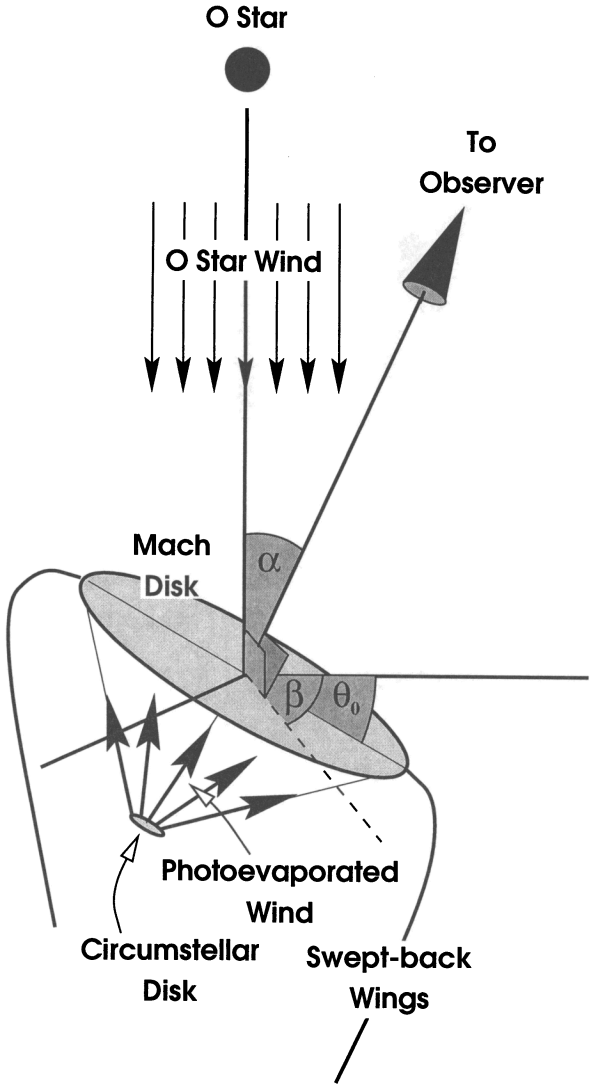

FIG. 13.—Geometry of the models, showing the orientation angles α and β, together with the disk inclination angle θ_0. The shock in the wind from θ^1C Ori is not shown for clarity.

the wind, this will never reduce the wind luminosity by more than a factor of about 2 unless λ is quite small.

Turning now to the contribution of the swept-back wings to the total emission, it is found that this is very sensitive to the assumptions made regarding the nature of the gas flow in the wings, in particular to how fast the thickness of the back-flowing gas layer increases with distance. As a simple approximation, we ignore the curvature of the wings and allow the gas to expand laterally at the sound speed. This leads to a thickness that increases linearly with distance along the wing at a rate inversely proportional to the Mach number of the gas. The gas density in the wings is then calculated by mass conservation, treating the velocity along the wings as a constant. The resultant emission measure decreases with distance along the wings to begin with, but eventually increases again when the thickness of the wings becomes comparable with their cylindrical radius. This is because the gas that approaches the axis is compressed to high densities by the convergent nature of the flow. This convergence occurs at a downstream distance of $\simeq 6$–$9D$ for $\lambda = 10$–300. If such a convergence occurs, then shocks will form and the flow will no longer be at all well described by our simple model. Notwithstanding these complications, we can calculate the luminosity of the portion of the wings where the emission measure is still declining (i.e., before the convergence on the axis becomes important) and derive the ratio of wing to Mach disk luminosity as $L_w/L_m \simeq 3$.

Hence, in general, the models predict a core-halo type morphology for the proplyds, with a central peak of emission, corresponding to the photoevaporated wind, surrounded by more extended, fainter emission from the Mach disk and wings, possibly with a further knot of emission downstream where the wings converge on the axis. Figures 11 and 12 show images of our proplyd model, calculated for $\lambda = 10$ and 30, respectively, for various values of the angle θ_0 between the disk normal and the direction to θ^1C Ori, and for various orientations with respect to the observer. The intensity scale of the images is logarithmic, spanning several orders of magnitude (see key to each figure) so that both high- and low-intensity features can be seen. Figure 13 illustrates the geometry of the models. The observer inclination angle α is the angle between the line of sight and the line joining the Proplyd to θ^1C Ori. The observer azimuthal angle β is the angle between the normal to these two lines and the plane that contains the normal to the circumstellar disk and the line joining the Proplyd to θ^1C Ori. The technique use to calculate the images is described in Henney (1996).

In all the models, the three emission components (wind, Mach disk, and wings) can be clearly seen. The ringlike appearance of the photoevaporated wind in some of the images is due to the occultation of the base of the wind by the stellar disk. All the models shown are inclined such that the observer sees the nonilluminated side of the circumstellar disk.

7. COMPARISON WITH OBSERVED Hα IMAGES

In Figure 14, we compare the models with Hα images of 11 proplyds observed with the Wide Field and Planetary Camera 2 (WFPC2) of the *HST* (C. R. O'Dell 1995, private communication). We have labeled the different proplyds following the notation of O'Dell & Wen (1994). For each proplyd, the top panel shows the observed image, which has been rotated so that the positive horizontal axis points toward θ^1C Ori and from which the nebular background has been removed. The middle panel shows a model image, scaled to the same size as the observations and smoothed by convolution with a Gaussian of FWHM 0.″23, so as to simulate the instrumental profile of WFPC2. The bottom panel shows the integrated brightness profile of the proplyd (*histogram*) together with that of the model (*solid line*). This brightness profile is calculated for each point along the horizontal axis by integrating the intensity along a line parallel to the vertical axis. The instrumental profile is shown by a dashed line in each case. The parameters of the model fits are shown in Table 1. The model fits shown are only meant to be illustrative, since an exhaustive search of parameter space was not performed (for example, only two values for λ, 10 and 30, were considered). However, several interesting conclusions can be drawn from the fits.

7.1. *The Proplyd Heads*

It is rather difficult for our models to produce the crescent-shaped head that is seen in several of the sources

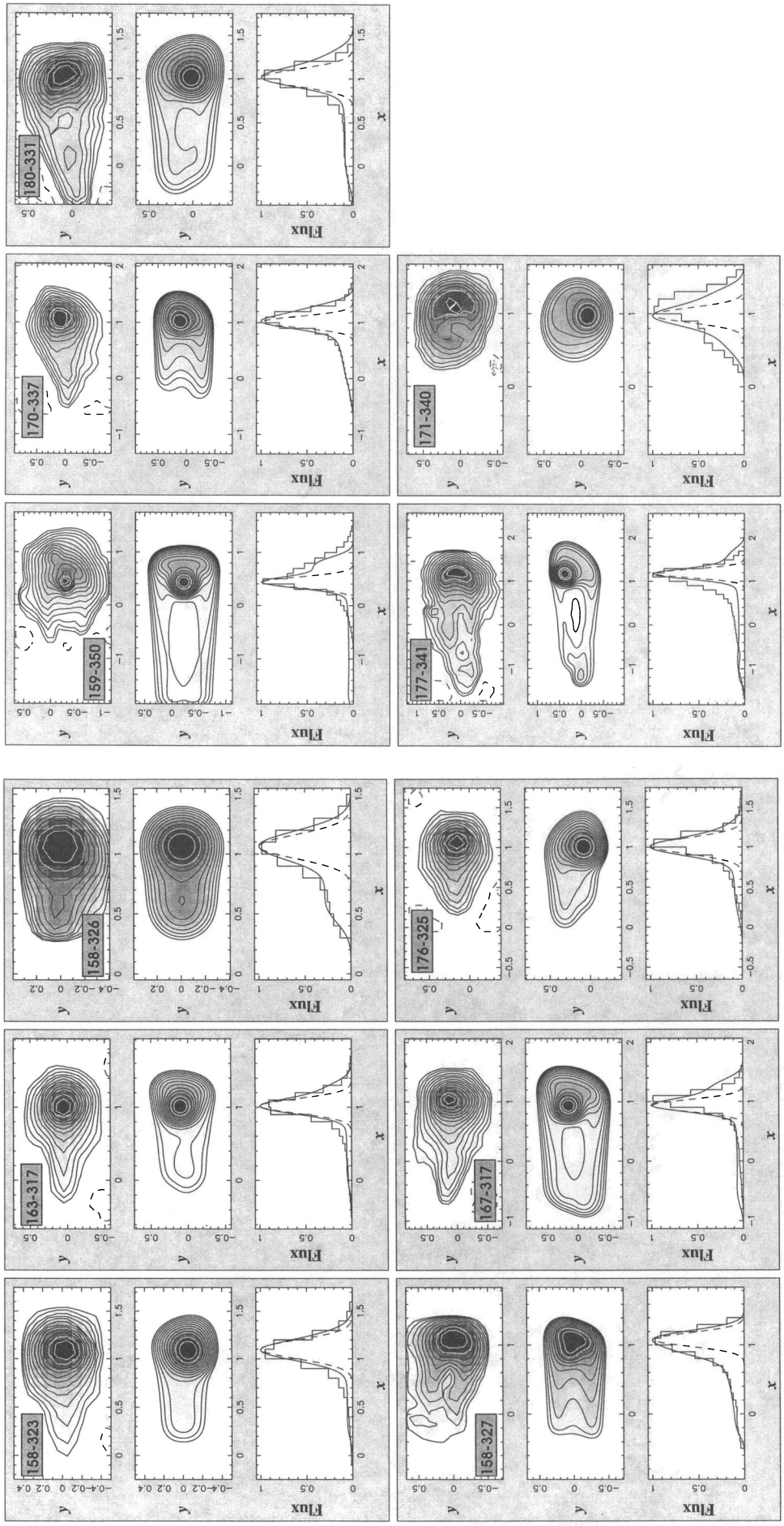

FIG. 14.—Model fits to *HST* images of proplyds. For each proplyd, the upper panel shows the background-subtracted *HST* image, while the central panel shows the fitted model. The axes are labeled in arcsec, and the interval between adjacent contours is $2^{1/2}$ for both the observed and model images. The highest two contours are drawn in white so as to be seen more clearly against the gray-scale image, which is linear in each case. The lower panel for each proplyd shows integrated brightness profiles in the *x*-direction, both for the observed image (*histogram*) and model (*solid line*). Also shown is the instrumental broadening used to convolve the models (*dashed line*; FWHM 0".23).

TABLE 1

MODEL FITS TO PROPLYD Hα IMAGE

PROPLYD[a]	OTHER NAMES[b]			MODEL PARAMETERS[c]					QUALITY OF FIT	
	HST	VLA	LV	λ	θ_0	α	β	r_d	Head	Wings
158−323.....	...	11	5	30	20	90	0	9.4	Good	Moderate
163−317.....	...	7	3	20	40	110	80	16.2	Good	Moderate
158−326.....	...	10	6	10	0	130	0	17.4	Good	Good
158−327.....	4	13	6	10	20	90	0	25.1	Good[d]	Good
167−317.....	...	6	2	30	20	130	40	21.5	Bad	Bad
176−325.....	...	2	...	30	40	130	0	10.5	Moderate	Moderate
159−350.....	3	9	...	30	0	110	0	25.7	Good	Bad
170−337.....	2	4	...	10	20	130	0	30.5	Good	Moderate[e]
180−331.....	...	19	...	30	20	130	0	14.8	Moderate	Moderate
177−341.....	1	1	...	30	30	140	0	23.3	Bad	Good[f]
171−340.....	11	...	...	10	40	170	0	27.1	Moderate	Moderate

[a] Coordinate-based designation (O'Dell & Wen 1994).
[b] HST: O'Dell et al. 1993. VLA: Felli et al. 1993. LV: Laques & Vidal 1979.
[c] θ_0, α, and β in degrees; r_d in a.u.
[d] Luminosity of model photoevaporated wind reduced by factor of 5.
[e] Model with nondiverging wings.
[f] Model wings converge on axis.

(158−326, 176−325, and 177−341). This is because the most luminous part of the model is the photoevaporated wind, which produces an emission peak some way back from the Mach disk. Note, however, that exactly this type of morphology is seen in one of the sources (159−350). For the case of 158−326, it is found that a satisfactory fit can be obtained by arbitrarily reducing the emission from the photoevaporated wind by a factor of 5. Such a reduction could be a result of additional absorbing material (dust or neutral gas) around the base of the wind, although this solution is admittedly ad hoc. The fit could possibly be further improved by including the small curvature of the Mach disk (see § 4.2). For 177−341, no such an adjustment is attempted, and hence, the fit to the proplyd head is rather poor. Note that the possible contribution of the central star itself to the flux in the Hα filter is not included in the model images.

7.2. *The Proplyd Tails*

Since the tails of the proplyds are fainter than the heads, their morphology is less reliably determined by the observations, especially in those objects seen superimposed on a strong, highly inhomogeneous background (158−323, 158−326, 158−327, 159−350). Additionally, the calculation of the tail morphology and emission is the least certain part of our dynamic model (see § 6). As a result of both these factors, we would ascribe less significance to the success or failure of the model fits in the tail region.

These caveats aside, there seem to be significant similarities and differences between the observations and the model fits. On the positive side, the models can easily reproduce both single- and double-tailed morphologies, as seen in the observations. On the other hand, the single tails seen in the observations generally lie on the horizontal axis through the proplyd center, whereas, in the models, they are more often to one side (e.g., 158−326). Also, although the observations show a steady decrease in the brightness of the tails as one moves further back from the head, in many of the models the brightness sharply falls just behind the central peak, followed by a flat plateau of constant brightness wings. The model fits to 158−323, 163−317, 167−317, 159−350, 180−331, and 177−341 all suffer from this deficiency, which is most easily seen in the integrated intensity profiles (bottom panels). In the case of 170−337, however, a much better fit to the integrated intensity profile is obtained by adopting a model in which the gas in the swept-back wings is confined to a thin layer, instead of expanding toward the axis, as in the canonical model. However, there is little justification for this, and the resultant two-tailed morphology is not observed in the object.

An interesting feature of the 177−341 image is the bright knot that appears at the "end" of the tail. This is very similar to the behavior of our models if we adopt a smaller cutoff radius for the convergence of the wings on the axis (see discussion in § 6). It results from the lateral inward expansion of the back-flowing wings and, although we have not attempted to model this, would be expected to result in a shock, followed, possibly, by a jetlike flow directed along the axis away from θ^1C Ori. It is fascinating to note that such a "jet" is indeed observed (O'Dell & Wen 1994) to leave 177−341 in this direction, extending all the way toward the region near HH 203, nearly 2′ away.

Although the proplyd 171−340 is very different in appearance from the other members of our sample, showing a more nearly circular morphology, we find that it can be fit reasonably well with our model if the inclination angle α is high. This would also imply that the actual distance of this proplyd from θ^1C Ori is some 5 times larger than the projected distance of 20″, which may account for the low luminosity of this object (see Fig. 10).

7.3. *Derived Model Parameters*

The derived parameters for the model fits are listed in Table 1. Since the fits are by no means unique, they should not be taken too seriously. It is interesting to note, however, that all the models have an orientation angle $\alpha \geq 90°$, implying that the proplyds are all nearer to the observer than θ^1C Ori. This is a consequence of the fact that in models with $\alpha < 90°$ there is no occultation of the photoevaporated wind by the circumstellar disk and, as a result, the photoevaporated wind is too bright to give a good fit to the observations. However, reducing λ below 10 (the lowest

value used in the models) may allow satisfactory fits to be obtained for $\alpha < 90°$. This is not attempted here since $\lambda = 10$ is already at the low end of the allowed range for our analytic model (see § 5). The second orientation angle β (see Fig. 13) was set to zero in most of the fitted models, since the variety of morphologies shown by models with $\beta = 0$ is not greatly less than the variety shown by all models (see, for example, Figs. 11 and 12, where the first two columns show models with $\beta = 0$).

The inclination angle of the circumstellar disk θ_0 can be seen to take a range of values $\leq 40°$. Models with $\theta_0 > 40°$ tend to be too asymmetrical to fit the observations well. As mentioned in § 4.4, our treatment of the proplyd wings is only valid for $\theta_0 \leq 60°$. For inclination angles larger than that, the swept-back wings would interact with the photoevaporated wind in a complicated way that cannot be captured by our simple model. However, one would expect the qualitative appearance of the proplyds to be similar.

The disk radii r_d shown in Table 1 are in the range 10–30 a.u. While the top end of this range is feasible for circumstellar disks around low-mass stars, the lower end is rather troublesome. Indeed, for three of our sample, 158−323, 167−317, and 159−350, the derived r_d is smaller than the critical radius r_c derived in § 5 (where we take the stellar masses from McCaughrean & Stauffer 1994, assuming an age of 3×10^5 yr). In such cases, the assumptions behind the photoevaporated wind model developed in § 4.1 are no longer even approximately valid. A wind solution would still be possible, but the effect of gravity would move the critical point away from the base of the wind, greatly reducing the mass-loss rate. This would probably push the system into the "choked" subsonic regime (§ 3), even for quite large values of λ. Hence, the model fits to these three proplyds are invalid, since the fitted parameters undermine the model assumptions.

8. CONCLUSIONS

In this paper, we have developed a two-wind interaction model for the compact emission-line objects (proplyds) in the Orion nebula. In this model, the ionizing radiation from θ^1C Ori drives a photoevaporated flow from the surface of accretion disks around young low-mass stars and this flow, in turn, interacts with the fast stellar wind from θ^1C Ori. The dynamics of the two-wind interaction has been calculated analytically, subject to various simplifying assumptions, and the emission properties of the models have been derived and compared in a detailed fashion with *HST* observations.

The models are found to show a broad qualitative resemblance to the observed morphologies of the proplyds (§ 7), although detailed comparison reveals some significant differences. The basic head-plus-tail appearance is well reproduced, but the morphology of the head region of the models is typically of the core-halo type, as opposed to the bow shock or arclike appearance of many of the observations (which can only be reproduced in the models by ad hoc adjustments to the relative brightnesses of the model components). Both double- and single-winged tails are seen in the models, as in the observations, although the models are typically more asymmetric. It is found (§ 5) that the observed Hα luminosities and sizes of the proplyds, as well as the dependence of these quantities on the distance between the proplyd and θ^1C Ori, can be well reproduced by the models, although the required circumstellar disk radii are somewhat larger than those inferred from the detailed fits of § 7.

High-resolution long-slit spectroscopic observations in the vicinity of the proplyds (Meaburn 1988; Meaburn et al. 1993; Massey & Meaburn 1993) reveal high-speed emission components in the [O III] λ5007 line, reaching velocities of order 100 km s^{-1} with respect to the bulk of the nebular emission. Although the brightest of these features, mainly associated with particular LV knots, are redshifted (receding), more sensitive observations (Massey & Meaburn 1993) also reveal an impressive complex of blueshifted (approaching) features with the curious property that the maximum velocity decreases with distance from θ^1C Ori. Given the fact that the derived parameters of our model fits suggest that the proplyds may all be on the near side of θ^1C Ori ($\alpha \geq 90°$, see § 7.3), then it would seem that this latter population of blueshifted features could be due to the emission from the proplyd wings. However, counting against this hypothesis is the fact that of the three proplyds (158−323, 163−317, and 167−317) common between our sample (see Table 1) and the above observations, in two cases the high-velocity emission is predominantly redshifted. The true situation is undoubtedly complicated, but it would be interesting to establish whether the majority of the observed emission features can be explained by the proplyds without having to posit a separate population of high-velocity jets.

One component that has been neglected in the calculations of the emission from our model has been the bow shock in the wind of θ^1C Ori. It would be comforting to associate this bow shock with the arclike features seen in the *HST* [O III] images between some of the proplyds and θ^1C Ori, but two arguments stand in the way of such an identification. First, by comparison with highly supersonic flows past blunt bodies (Van Dyke 1982), the standoff distance between the Mach disk in the photoevaporated wind and the bow shock in the wind from θ^1C Ori should be very small. Second, for such high velocities as are expected for the θ^1C Ori wind, the postshock ionization state would be very high and little [O III] emission would be produced. However, if the θ^1C Ori wind were to be modified by the hydrodynamic or photoevaporative ablation of clumps (Hartquist et al. 1986; Arthur, Dyson, & Hartquist 1993; Lizano et al. 1996), then the wind velocity could be substantially reduced before shocking against the proplyds. This mass loading would circumvent both of the above objections, increasing the standoff distance due to the decreased Mach number and augmenting the emission of optical lines in the postshock region due to the reduced postshock temperature. It should also be noted that, since mass loading conserves the momentum flux in the wind, the analysis of §§ 3 and 4 would be unaffected. Although such a hypothesis remains unproven, it is perhaps worthy of further investigation.

In summary, we feel that the model presented in this paper, although somewhat crude, is moderately successful in explaining the observed shapes of the proplyds. The basic idea for explaining emission-line knots in H II regions, that of the photoevaporation of neutral material, is certainly not new and can be traced back as far as Dyson (1968). Indeed, the idea that the source of this neutral material may be circumstellar disks around low-mass stars has also been entertained in many previous works (Churchwell et al. 1987; O'Dell, Wen, & Hu 1993; Stauffer et al. 1994; McCul-

lough et al. 1995). However, we believe that this is the first time that the consequences of such a model have been worked out in any detail and certainly the first time that detailed comparisons with the morphology of individual proplyds have been made. A more stringent test of this model, or any other, would be a detailed comparison with high-resolution emission-line spectroscopy of the proplyds. Such work is in progress.

We are extremely grateful to R. O'Dell for sending us his unpublished *HST* observations, and we thank J. Cantó for useful discussions.

REFERENCES

Arthur, S. J., Dyson, J. E., & Hartquist, T. W. 1993, MNRAS, 261, 425
Bohlin, R. C., & Savage, B. D. 1981, ApJ, 249, 109
Cardelli, J. A., & Clayton, G. C. 1988, AJ, 95, 516
Churchwell, E., Felli, M., Wood, D. O. S., & Massi, M. 1987, ApJ, 321, 516
Conti, P. S. 1973, ApJ, 179, 161
Courant, R., & Friedrichs, K. O. 1948 Supersonic Flow and Shockwaves (New York: Interscience)
Dyson, J. E. 1968, Ap&SS, 1, 388
Felli, M., Taylor, G. B., Catarzi, M., Churchwell, E., & Kurtz, S. 1993, A&AS, 101, 127
Hartquist, T. W., Dyson, J. E., Pettini, M., & Smith, L. J. 1986, MNRAS, 221, 715
Henney, W. J. 1996, Rev. Mexicana Astron. Astrofis., 32, 3
Howarth, I. D., & Prinja, R. K. 1989, ApJS, 69, 527
Lacques, P., & Vidal, J. L. 1979, A&A, 73, 97
Leitherer, C. 1988, ApJ, 326, 356
Leroy, J. L., & Le Borgne, J. F. 1987, A&A, 186, 322
Lizano, S., Cantó, J., Hollenbach, D., & Garay, G. 1996, ApJ, in press
Massey, R. M., & Meaburn, J. 1993, MNRAS, 262, L48
Mathis, J. S., Perinotto, M., Patriarchi, P., & Schiffer, F. H., III. 1981, ApJ, 249, 99
Meaburn, J. 1988, MNRAS, 233, 791
Meaburn, J., Massey, R. M., Raga, A. C., & Clayton, C.A. 1993, MNRAS, 260, 625
Menten, K. M., & Reid, J. M. 1996, in preparation
McCaughrean, M. J., & Stauffer, J. R. 1994, AJ, 108, 1382
McCullough, P. R., Fugate, R. Q., Christou, J. C., Ellerbroek, B. L., Higgins, C. H., Spinhirne, R. A., Cleis, R. A., & Moroney, J. F. 1995, ApJ, 438, 394
O'Dell, C. R., Walter, D. K., & Dufour, R. J. 1992, ApJ, 399, L67
O'Dell, C. R., & Wen, Z. 1994, ApJ, 436, 194
O'Dell, C. R., Wen, Z., & Hu, X. 1993, ApJ, 410, 696
Panagia, N. 1973, AJ, 78, 929
Panagia, N., & Felli, M. 1975, A&A, 39, 1
Pastor, J., Cantó, J., & Rodríguez, L. F. 1991, A&A, 246, 551
Patriarchi, P., & Perinotto, M. 1985, A&A, 143, 35
Stauffer, J. R., Prosser, C. F., Hartmann, L., & McCaughrean, M. J. 1994, AJ, 108, 1375
Van Dyke, M. 1982, An Album of Fluid Motion (Stanford: Parabolic Press)